Ground-Motion Modeling of the 2016 Mw 6.2 Amatrice, Italy, Earthquake, by a Broadband Hybrid Kinematic Approach, Including Empirical Site Effects

Article *in* Seismological Research Letters · July 2024

DOI: 10.1785/0220230409

5 authors, including:

František Čejka
Charles University in Prague

Sara Sgobba
National Institute of Geophysics and Volcanology

Francesca Pacor
National Institute of Geophysics and Volcanology

František Gallovič
Charles University in Prague

Ground-Motion Modeling of the 2016 M_w 6.2 Amatrice, Italy, Earthquake, by a Broadband Hybrid Kinematic Approach, Including Empirical Site Effects

František Čejka*[1], Ľubica Valentová Kristeková[1], Sara Sgobba[2], Francesca Pacor[2], and František Gallovič[1]

Abstract

The region of Central Italy is well known for its moderate to large earthquakes. Events such as the 2016 M_w 6.2 Amatrice earthquake generated in the shallow extensional tectonic regime motivate numerical simulations to gain insights into source-related ground-motion complexities in the near-source region. We utilize a hybrid integral-composite kinematic rupture model by Gallovič and Brokešová (2007) to simulate the Amatrice earthquake in a broadband frequency range (up to 10 Hz). In the first step, we optimize the input source parameters using a grid-search method by minimizing the spectral acceleration bias between synthetic and recorded strong-motion data at reference rock stations within 50 km of the source. To verify the robustness of the optimal model, we simulate the ground motions at 400 virtual stations and compare their spectral accelerations with the predictions of an empirical nonergodic ground-motion model (GMM) for rock sites in Central Italy (Sgobba *et al.*, 2021). The synthetics show a good agreement with the empirical model regarding both median and variability. Finally, we account for local site effects at nonreference stations by combining the simulations on rock with empirical site terms derived by the nonergodic GMM. The site-corrected spectral responses generally improve the match with the observations, demonstrating a successful fusion of numerical simulations with empirical estimates toward reproducing near-source ground motions.

Cite this article as Čejka, F., Ľ. Valentová Kristeková, S. Sgobba, F. Pacor, and F. Gallovič (2024). Ground-Motion Modeling of the 2016 M_w 6.2 Amatrice, Italy, Earthquake, by a Broadband Hybrid Kinematic Approach, Including Empirical Site Effects, *Seismol. Res. Lett.* **XX**, 1–14, doi: 10.1785/0220230409.

Supplemental Material

Introduction

The Central Italy region is well known for its relatively large seismicity and complex tectonic structure. It features mainly seismogenic north-northwest–south-southeast oriented structures driven by the extensional tectonic regime of the Central Apennines. Many damaging earthquakes struck this area over the last centuries, the most recent being the 2009 M_w 6.3 L'Aquila event and the 2016–2017 Amatrice–Visso–Norcia seismic sequence. This sequence was initiated by the M_w 6.2 Amatrice earthquake on 24 August 2016, 01:36 UTC, with the most devastating consequences, causing 299 fatalities, building collapses, and damage with macroseismic intensities up to XI (Galli *et al.*, 2016). The earthquake ruptured northwest–southeast oriented normal fault located in the southeast bend of the Sibillini Thrust which is a main compressional structure in the area (Pizzi *et al.*, 2017; Fig. 1a). Given the significance of this event, several studies in the literature have focused on the implementation of advanced simulation techniques to generate synthetic waveforms in a broad frequency range, for example, with hybrid methods (Pischiutta *et al.*, 2016, 2021), or dynamic models (Gallovič *et al.*, 2019; Taufiqurrahman *et al.*, 2023; Gallovič and Valentová, 2023).

The physics-based ground-motion simulations are a promising tool to fill the observational gaps in the near-source region (Ameri *et al.*, 2012; Bradley *et al.*, 2017; McCallen *et al.*, 2021; Paolucci *et al.*, 2021; Pitarka, Akinci, *et al.*, 2021; Pitarka, Graves, *et al.*, 2021; Valentová *et al.*, 2021), connecting various source-related complexities, such as the distribution of slip, rupture time, rise time, with peculiar features of the spatial distribution of observed shaking due to radiation pattern and directivity.

1. Department of Geophysics, Faculty of Mathematics and Physics, Charles University, Prague, Czech Republic, https://orcid.org/0000-0001-6418-0029 (FC); https://orcid.org/0000-0002-9574-1105 (ĽVK); https://orcid.org/0000-0002-9268-3923 (FG); 2. Istituto Nazionale di Geofisica e Vulcanologia, Milan, Italy, https://orcid.org/0000-0002-5669-8650 (SS); https://orcid.org/0000-0001-5745-0414 (FP)

*Corresponding author: cejka@karel.troja.mff.cuni.cz

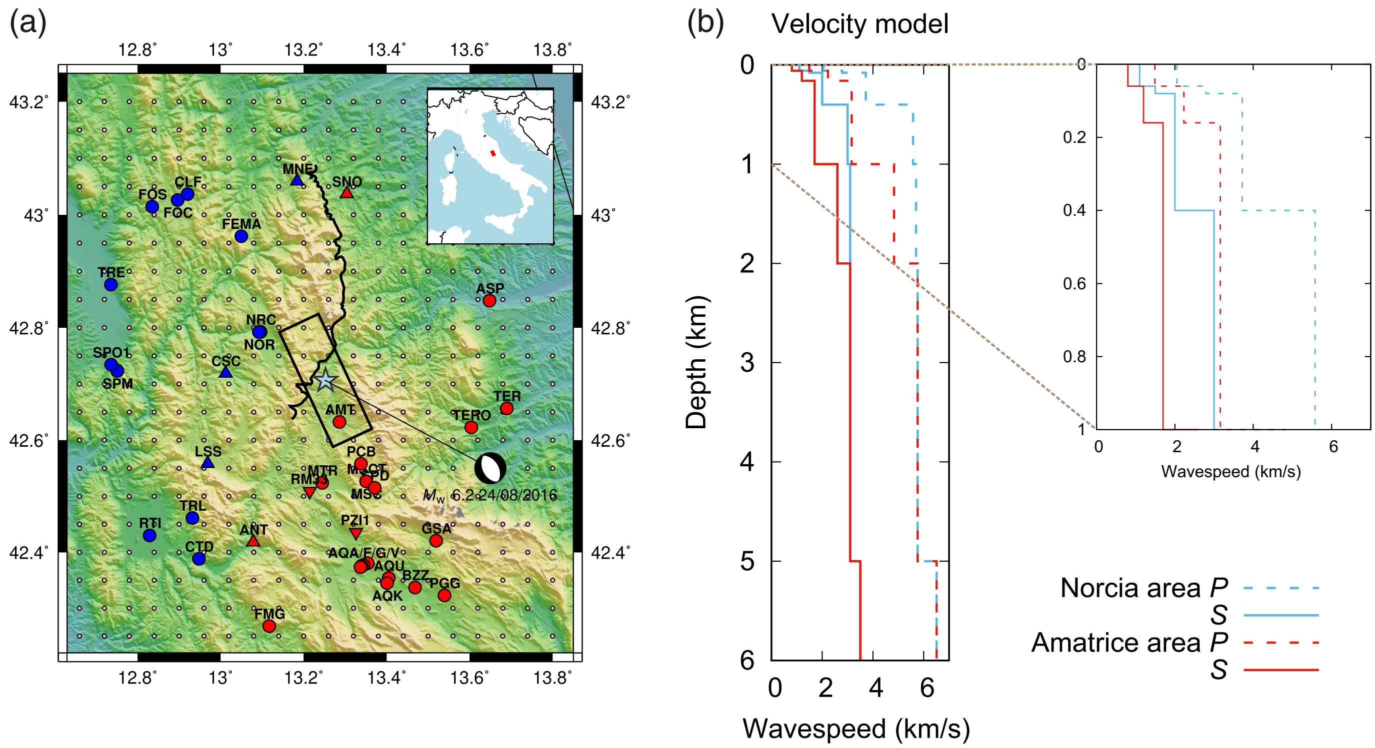

They can also complement the empirical ground-motion models (GMMs) that are one of the main prediction tools used in seismic hazard assessment, especially in the epicentral areas, and for evaluating the seismic response of strategic structures such as power plants, infrastructure, or buildings in urban areas. For example, the so-called hybrid simulations are employed frequently due to their efficiency in a broad frequency range (Mai and Beroza, 2003; Gallovič and Brokešová, 2007; Graves and Pitarka, 2010; Graves *et al.*, 2011; Paolucci *et al.*, 2018). The hybrid methods combine the high-frequency stochastic approaches (e.g., von Karman distributions) with the deterministic rupture models at low frequencies that may come from kinematic source inversions (Ameri *et al.*, 2012; Razafindrakoto *et al.*, 2018; Ojeda *et al.*, 2021; Pischiutta *et al.*, 2021) or even dynamic source modeling (Akinci *et al.*, 2017). Unlike the empirical GMM, the ground-motion simulations can provide a three-component time series comprising complex source and propagation effects. Yet, their results need to be validated against observations to simulate reliable ground shaking.

In this work, we simulate broadband (up to 10 Hz) strong ground motions of the M_w 6.2 Amatrice earthquake using the Hybrid Integral-Composite (HIC) kinematic model of a finite-extent rupture introduced by Gallovič and Brokešová (2007). The wave propagation is implemented by numerical calculation of synthetic Green's functions (GF) in regional 1D crustal velocity models in a broad frequency range. The HIC approach was previously validated by modeling several strong earthquakes, for example, the 1980 M_w 6.9 Irpinia, Central Italy (Ameri *et al.*, 2011), the 2009 M_w 6.3 L'Aquila, Central Italy (Ameri *et al.*, 2012), the 2011 M_w 7.1 Van, eastern Türkiye (Gallovič *et al.*, 2013), or recently the 2023 M_w 7.8 Kahramanmaraş, Türkiye (Čejka *et al.*, 2023) earthquakes.

Figure 1. Study area and velocity models. (a) Epicentral area of the 2016 Amatrice earthquake. The fault plane adopted from Pizzi *et al.* (2017) is shown by the black rectangle. Network stations are shown by triangles and circles, color coded by the adopted crustal model: The circles correspond to the nonreference station, triangles to the reference stations with all components used in the model optimization, and inverted triangles depict stations for which only vertical components are considered in the optimization. The faulting mechanism and centroid location are shown by the focal mechanism plot (Istituto Nazionale di Geofisica e Vulcanologia [INGV]-webservice). Mainshock epicenter (light blue star) is adopted from the relocated catalog by Chiaraluce *et al.* (2017). The black curves correspond to the Sibillini Thrust separating different crustal regimes of the Norcia and Amatrice area. The pink circles are 400 virtual stations used for comparison with a ground-motion model (GMM). The inset shows a map of Italy with the study area depicted by a red rectangle. (b) Velocity models used to calculate Green's functions for stations in the Norcia (blue) and Amatrice (red) area, see also Table S1. The models coincide below 2 km. The inset zooms in the uppermost 1 km. The color version of this figure is available only in the electronic edition.

In the first step, we calibrate source-related parameters of the HIC method on a set of reference stations best matching the observed data given a specific metric (Graves and Pitarka, 2010; Ojeda *et al.*, 2021). In this primary calibration phase, in addition to the metric adopted to assess the goodness of fit of the model, the choice of the reference sites also plays a critical role, given the complexity of the geomorphological setting in

Central Italy (Felicetta *et al.*, 2021, and references therein). In this case, the number of reference stations is limited and thus two validation exercises are performed to support the applicability of the optimal source model: (1) comparison of the simulated ground motions of the 2016 Amatrice earthquake on a dense set of virtual rock-site stations with the predictions of regional nonergodic GMM (SEA21, Sgobba *et al.*, 2021), and (2) comparison of ground motions with the recordings at nonreference stations with significant site effects, representing additional observations independent of the optimization process. As for the latter, we correct the synthetic acceleration spectra simulated on rock by empirical site amplification functions derived from nonergodic GMM calibrated in Central Italy (Sgobba *et al.*, 2024).

This work, in addition to validating the broadband source model of the 2016 Amatrice earthquake on a smaller set of reference stations, follows a more systematic approach by integrating empirical amplification functions in numerical simulations over a more comprehensive data set in a broad frequency range, taking advantage of the complete consistency in modeling assumptions. Our study, therefore, aims to propose a methodological example for correcting the simulated ground motions on rock with the repeatable site contributions of nonergodic GMM to reproduce the ground motions on generic sites. This task is very challenging and thus possible only in densely monitored areas and with good empirical estimates, such as Central Italy.

Data and Methods

Near-source recordings

Because of the frequent seismicity, the Central Apennines in Italy are well covered by seismic stations belonging to the National Accelerometric Network (code IT, operated by the Italian Department of Civil Protection) and the National Seismic Network (code IV, operated by the Istituto Nazionale di Geofisica e Vulcanologia). The Amatrice earthquake was recorded by 38 accelerometric stations of the IV and IT permanent networks within 50 km of the epicenter (Fig. 1a), see Data and Resources. For the model calibration, we choose seven reference stations with weak or no site amplifications selected using the multiproxy technique reference rock identification method (RRIM) developed by Lanzano *et al.* (2020, 2022) (colored triangles in Fig. 1a). This approach identifies reference recording stations on the base of several proxies for the site response, related both to the analysis of geophysical and seismological data and to the geomorphological features of the site. Almost all the selected reference stations are installed on rigid soils with V_{S30} varying in the 550–1100 m/s range and are free from resonance phenomena (see Table S1, available in the supplemental material to this article).

The reference sites considered in the model optimization comprise two groups: the first contains five stations, already identified as reference in Lanzano *et al.* (2022), for which all the three components are used (LSS, MNF, ANT, SNO, and CSC; upside triangles in Fig. 1a); the second group includes two additional stations, for which we consider only the vertical components, (PZI1, RM33; inverse triangles in Fig. 1a). Although they do not exhibit prominent amplifying effects, they do not exceed the minimum score selected in the RRIM methodology to be classified as good reference sites. They were included in the optimization to improve the azimuthal coverage toward the south.

We filter all recordings by a Butterworth filter between 0.05 and 10 Hz.

Source model

In the HIC technique, the rupture process is represented by overlapping rectangular subsources randomly distributed on the fault with fractal number-size distribution, in which the number of subsources decreases linearly with increasing subsource size. The subsources are characterized by a constant stress-drop scaling, composing a slip distribution with k^{-2} decay at high wavenumbers k. These subsources are treated differently in the low- and high-frequency ranges, and each of these procedures results in a seismogram in partially overlapping frequency bands. Here, we explain the two methods in more detail (see also Gallovič and Brokešová, 2007):

- Up to f_2, the *integral* of the representation theorem is calculated: The fault is discretized to a regular grid of subfaults. At each subfault, the slip is computed as a sum of contributions from all subsources covering the subfault. The rupture time is calculated from the distance of the point to the nucleation point and the prescribed (constant) rupture velocity. The slip velocity function has Brune's pulse shape with constant rise time. The synthetic waveforms are obtained by convolving slip rates with GFs, calculated from the center of each subfault, and subsequently summing all subfaults' contributions over the fault. The advantage of this approach is that the directivity of the rupture propagation is well captured at lower frequencies due to the coherent summation of the subfaults' wavefield contributions.
- Above f_1, the *composite* approach is used: The individual subsources are treated as point sources with Brune's source time function, described by their respective seismic moments and corner frequencies (assuming the constant stress drop). In addition, we allow a random variation in the mechanism of the subsources to weaken the radiation pattern at high frequencies. Synthetics for a given subsource are obtained by convolution of the Brune source time functions (Brune, 1970) with GFs calculated from the subsources' centers. These contributions are then shifted in time by their respective rupture times, calculated as the time the rupture needs to reach the subsource, considering a constant rupture velocity. All the subsources' contributions are then summed. In contrast to the integral part, the directivity effect is suppressed due to the incoherent summation of the subsources' wavefield contributions.

The crossover frequency section (f_1, f_2) is treated in the Fourier domain by weighted averaging of the real and imaginary parts of the two seismograms from the two approaches using $\cos^2$ and $\sin^2$ functions as weights. Because the low- and high-frequency synthetics are based on the same subsource distribution and synthetic GFs, the crossover combination does not require any specific manual fine-tuning.

The subevents' corner frequencies are adjusted so that the resulting high-frequency acceleration plateau of the event has a prescribed height. For the omega-square source model, the height of the acceleration spectral plateau is equal to $M_0\hat{f}_c^2$ with M_0 and $\hat{f}_c$ being the total scalar seismic moment and the event corner frequency, respectively. In the HIC model, we generalize the corner frequency as

$$\hat{f}_c = \frac{av_r}{\sqrt{LW}}, \tag{1}$$

in which L and W are the rupture length and width, respectively; v_r is the rupture velocity; and parameter a is a parameter controlling the strength of the high-frequency radiation, with a value close to 1 as suggested by previous studies (Gallovič and Brokešová, 2007; Ameri *et al.*, 2009, 2011; etc.).

To validate the HIC source model for the Amatrice earthquake, we adopt a fixed fault plane, M_0 and subsource layout similar to the slip model from Bayesian dynamic source inversion by Gallovič *et al.* (2019). The optimization parameters are rupture velocity v_r and parameter a.

Crustal velocity models

To calculate the synthetic waveforms, we employ the synthetic GFs that were precalculated in the 1D velocity models using the Axitra code (Cotton and Coutant, 1997). The GFs are filtered in the frequency range 0.05–10 Hz, the same as used for the records.

We consider a specific 1D velocity model for each of the two major geological domains divided by the Sibillini Thrust, which is the main structural discontinuity in the area (Fig. 1a): (1) the south-southeast unit of the Sibillini Thrust, which lies on the Laga formation (Amatrice area) and (2) the carbonate unit to the north-northwest of the thrust (Norcia area). For the Amatrice area, we adopt the crustal velocity model proposed by Ameri *et al.* (2012) which showed a good fit between the observed and simulated ground motions for the 2009 L'Aquila earthquake. The crustal model was supplied by three subsurface layers in dynamic source modeling of the 2016 Amatrice earthquake by Gallovič and Valentová (2023) resulting in a good fit of broadband ground motions with both observations and regional GMM. For the Norcia area, we adapt the 1D velocity model of Bianchi *et al.* (2010) in the topmost kilometer by resampling the shear-wave array profile V_S performed at stations CSC (Cascia) and LSS (Leonessa). The results of the aforementioned geophysical measurements are available in the ITalian ACcelerometric Archive database (see Data and Resources). For the GF calculation, the fault is embedded completely in the northern and southern medium for northern and southern stations, respectively. However, because the two models differ only up to 2 km depth, in which almost no slip is generated, neglecting two different crustal models on the fault has negligible effect. The two velocity models proposed for the Amatrice and Norcia area are shown in Figure 1b and Table S2.

The anelastic attenuation is modeled by depth-dependent quality factor Q (see also Table S2 and Fig. S1) and high-frequency decay parameter κ (Anderson and Hough, 1984). Following Castro *et al.* (2022), we adopt $\kappa = 0.03$ s as a mean value for all the stations. The effect of different choice of κ on ground motion is explored in Text S1 and Figure S2.

Evaluation of the modeling performance

To assess the fit between the simulated ground motions and the observations, we adopt the method of Graves and Pitarka (2010). First, we evaluate the logarithm of the ratio between spectral acceleration (SA, 5% damping) of synthetic records and observed data,

$$r_j(T_i) = \ln\left(\frac{M_j(T_i)}{O_j(T_i)}\right), \tag{2}$$

in which $r_j(T_i)$ is an SA residual at each station's component j and period T_i, and O_j and M_j are observed and modeled SA responses, respectively. Then we compute the model's SA bias at each period as

$$B(T_i) = \frac{1}{N}\sum_{j=1}^{N} r_j(T_i), \tag{3}$$

in which N is the number of all site components considered in the model assessment.

The standard deviation $\sigma(T_i)$ is computed as

$$\sigma(T_i) = \left\{\frac{1}{N}\sum_{j=1}^{N}[r_j(T_i) - B(T_i)]^2\right\}^{1/2}. \tag{4}$$

To describe the model fit by a single number, B^2-value, we take the average of $B^2(T_i)$ over all the periods, that is,

$$B^2 = \frac{1}{M}\sum_{i=1}^{M} B^2(T_i), \tag{5}$$

in which M is the number of periods. The optimal model is chosen as the one with minimal B^2-value over the source parameters.

Here, we deviate from the standard approach of Graves and Pitarka (2010), in which the B-value is calculated as an average value of SA bias over all stations, periods, and components. In our experience, this can promote models that generate the positive and negative SA bias over different periods, still having the B-value close to zero. Contrarily, taking the B^2-value as in equation (5) guarantees that the optimal model provides SA bias close to zero over the whole inspected period range.

We also explore the variability of the SA bias using the mean σ^2-value defined as

$$\sigma^2 = \frac{1}{M}\sum_{i=1}^{M}\sigma^2(T_i). \quad (6)$$

In an ideal case, the minima in the B^2 and σ^2 values overlap, suggesting that the optimal model generates ground motions most similar to the observed ones not only in average over the reference stations, but also individually at each station (Gallovič, 2016).

Regional empirical GMMs

To validate our optimal source model, we use empirical GMMs in two ways: first, the simulated ground motions are validated against the GMM prediction using a grid of virtual rock sites; second, we combine empirical site-correction terms evaluated from the GMM at nonreference stations with the simulated ground motions on rock and compare them with the observations.

In particular, we compare the synthetic predictions from HIC with a fully nonergodic GMM calibrated specifically for Central Italy by Sgobba *et al.* (2021), referenced as SEA21. In this nonergodic model, the variability terms are decomposed via mixed-effect regression and geospatial analysis into systematic effects of the path ($\delta P2P$), site ($\delta S2S$), source zone ($\delta L2L$), and event-specific correction (δB_e). The residual term δW_0 accounts for all other (nonsystematic) effects.

To evaluate the empirical ground motion for the Amatrice earthquake at rock sites using SEA21, the median prediction is corrected by δB_e and $\delta L2L$ corrections specific to the Amatrice source. The corresponding standard deviation is then composed of the remaining variability terms due to the path (ϕ_{P2P}), the reference sites (ϕ_{S2Sref}), and aleatory standard deviation (ϕ_0). This process is used to ensure the best consistency between the empirical model and the numerically simulated features. For example, assuming the GMM generic median value without the event-specific correction can result in simulations overestimating the GMM because the Amatrice-specific correction is positive. On the other hand, assuming the complete variability in GMM (between- and within-event including nonreference sites) could be incorrectly interpreted as underprediction of variability in the simulated ground motions.

In the second step of our validation process, we aim to improve synthetic predictions at nonreference sites using empirical site functions named $\delta S2S$. These correspond to the systematic amplifications observed at generic sites over all the events when compared to the median GMM prediction at the reference-rock level. We evaluate these functions as random-effect terms of the regression model which lacks an explicit scaling trend with V_{S30}, hence, they can be considered as amplification factors of the site in comparison to the reference-rock condition. Therefore, these functions are ideal proxies for the site response, as suggested by Bard *et al.* (2020) and Loviknes *et al.* (2021). Here, instead of considering the $\delta S2S$ of Sgobba *et al.* (2021), which are based on a model calibrated on 36 reference sites, we prefer to adopt the site-to-site terms derived by Sgobba *et al.* (2024, SEA24) that are based on the same approach as SEA21 but calibrated only on six reference sites, including the three (LSS, MNF, and SNO) used in this study in the optimization of the source model. In this way, the reference-rock motions between the optimized simulations and the GMM predictions are consistent, facilitating the application of the SEA24 empirical site corrections to the synthetic spectra. Note that the synthetics are not corrected for other systematic terms, such as $\delta L2L$ and $\delta P2P$ because the kinematic simulations have already been optimized for the source, and the propagation terms are negligible in our frequency range.

Results

Optimal HIC model of the Amatrice earthquake

Following the kinematic and dynamic source models of Pizzi *et al.* (2017) and Gallovič *et al.* (2019), we set the strike/dip/rake angles to 155°/45°/−85°, the latitude, and longitude of the epicenter to 42.7063° N, 13.2532° E, and the scalar seismic moment to 2.6×10^{18} N · m. We resemble the best-fitting slip model of the dynamic source inversion by Gallovič *et al.* (2019) by fixing the fault dimension to 25×12 km^2 and randomly generating the subsources distribution considering the dynamic slip model as a spatial probability density function, see Figure 2a,c.

The crossover frequency range partitions the deterministic and stochastic rupture behavior and can be generally treated as a free parameter. To keep our validation simple, we adopt values that were found in a previous HIC application for an event of similar magnitude in Central Italy, the 2009 M_w 6.3 L'Aquila earthquake (Ameri *et al.*, 2012), that is, $f_1 = 0.15$ Hz and $f_2 = 0.6$ Hz. The crossover frequency range is presumably related to the corner frequency of the event (and thus magnitude) and covers the frequency band in which the source directivity is generally observed (Pacor *et al.*, 2016; Colavitti *et al.*, 2022). Nevertheless, the precise values of the crossover frequencies may be event-dependent; therefore, in Text S2 and Figure S3, we discuss the effects of different values on the modeling in more detail.

The rupture velocity v_r and parameter a are optimized with a grid-search method. For parameter a, we assume range 0.4–2.5, with step 0.1. The rupture velocity is varied between 1.7 and 3.7 km/s (close to the S-wave velocity), with a step of 0.1 m/s. The grid-search results over v_r and a in terms of the B^2-value and σ^2-value are shown in Figure 2b. The set of optimal models with lower B^2-values are distinguished in Figure 2b by the blue-colored region. The optimal model with minimal B^2-value is characterized by parameter a = 1.35 and rupture

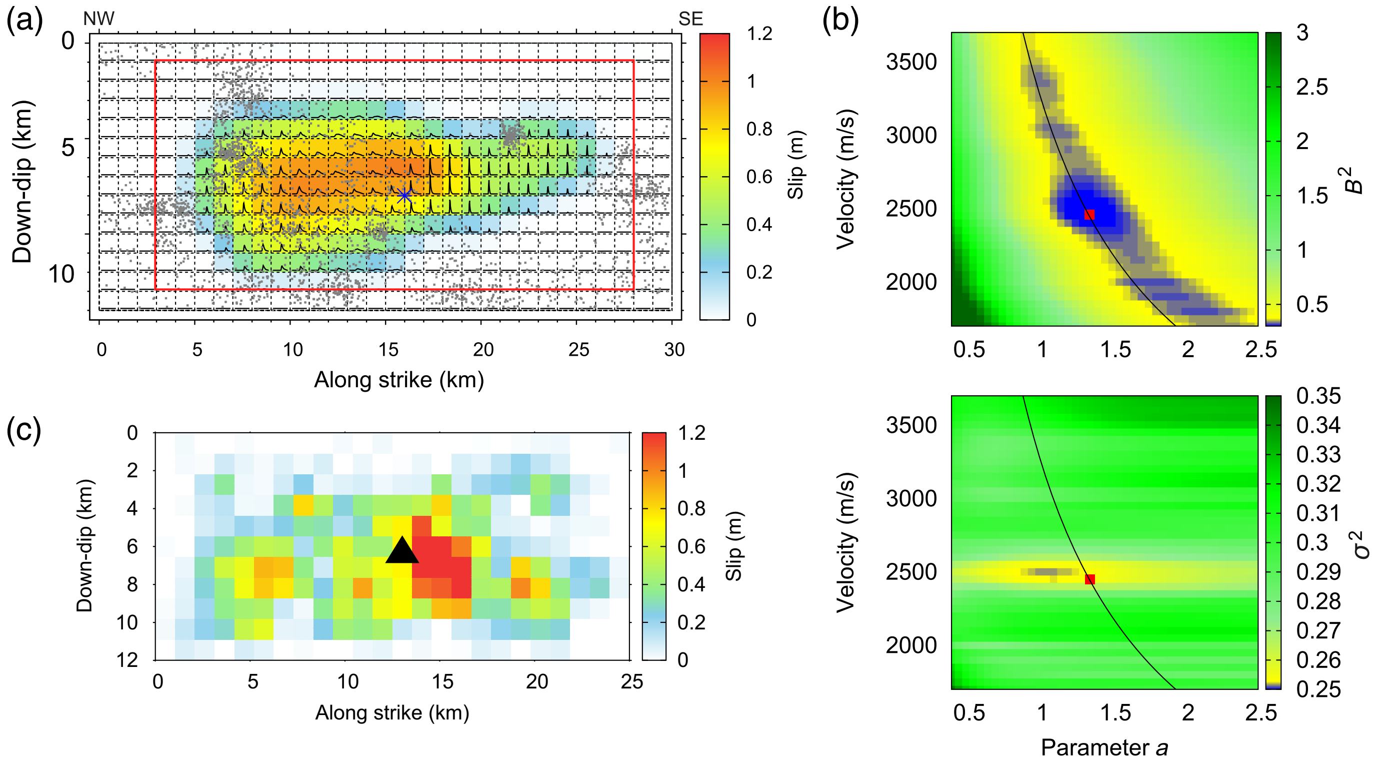

Figure 2. Slip model of the 2016 Amatrice earthquake and results of the optimization of the broadband model. (a) Slip distribution of the 2016 M_w 6.2 Amatrice earthquake from the dynamic source inversion by Gallovič *et al.* (2019). The blue star is the nucleation point, gray dots are aftershocks. The red rectangle depicts the area utilized in the Hybrid Integral-Composite (HIC) modeling. (b) Result of the grid search over parameters a and v_r for an optimal model of the 2016 Amatrice earthquake in terms of B^2 (top) and σ^2 (bottom) values (see equations 2–6). The red square shows the model with minimal B^2 with $v_r = 2.45$ km/s and a = 1.35. The black line delineates models with the same corner frequency f_c as the optimal model (see equation 1). (c) Slip distribution generated for the broadband modeling based on probability density in panel (a). The black triangle is the nucleation point. The color version of this figure is available only in the electronic edition.

velocity $v_r = 2.45$ km/s, slightly slower than in other studies (Tinti *et al.*, 2016; Cirella *et al.*, 2018; Gallovič *et al.*, 2019).

The plot of the B^2-value in Figure 2b exhibits a clear trade-off between parameters a and v_r. This trade-off can be explained by the pivotal role of corner frequency f_c in the waveform modeling (see equation 1). In our model, the corner frequency is also related to the so-called stress parameter, $\Delta\sigma = \frac{7}{16}\left(\frac{f_c}{0.37 v_s}\right)^3 M_0$, characterizing the high-frequency acceleration plateau. The optimal model has a corner frequency of 0.19 Hz and stress parameter of 3.6 MPa. Figure 2b shows the line of constant corner frequency following equation (1), showing perfect agreement with the valley of low B^2-values. We note that our corner frequency and stress parameter are similar or lower than the empirical estimates for the Amatrice earthquake derived from empirical studies ranging 0.2–0.35 Hz and 3.4–9 MPa, respectively (Gallovič *et al.*, 2019; Morasca *et al.*, 2019; 2022; Supino *et al.*, 2019; Kemna *et al.*, 2021; Calderoni and Abercrombie, 2023).

The σ^2-value representing the mean variability of the SA residuals in Figure 2b shows very low sensitivity to parameter a, but a very clear minimum in v_r around 2.5 km/s. The source model with minimal σ^2-value underestimates the observed ground motions due to the too low value of parameter a and thus has a significantly higher B^2-value (0.3786 compare with 0.2841 of the optimal model). On the other hand, the source model with minimal B^2-value has the σ^2-value only slightly higher than the minimum (0.2543 compare with 0.2516), thus matching not only the SA averaged over the stations, but also suggesting that this optimal model belongs to those with low variability in the SA bias (the yellow region in Fig. 2b bottom). The dependence of σ^2 primarily on v_r is related to the rupture directivity effect affecting the variability of ground motions in different azimuths, unlike parameter a that affects all stations equally.

Figure 3a shows the period-dependent componentwise SA bias (equation 3) for the optimal model for the individual reference stations together with its mean and standard deviation. The mean SA bias is close to zero, showing a generally good fit between the simulations and observations on reference stations. The variability of the SA residuals (gray and red dashed lines in Fig. 3a) generally decreases with increasing period, suggesting that the optimal HIC source model well represents the large-scale features. On the other hand, the increase of the variability toward the short periods (i.e., high frequencies)

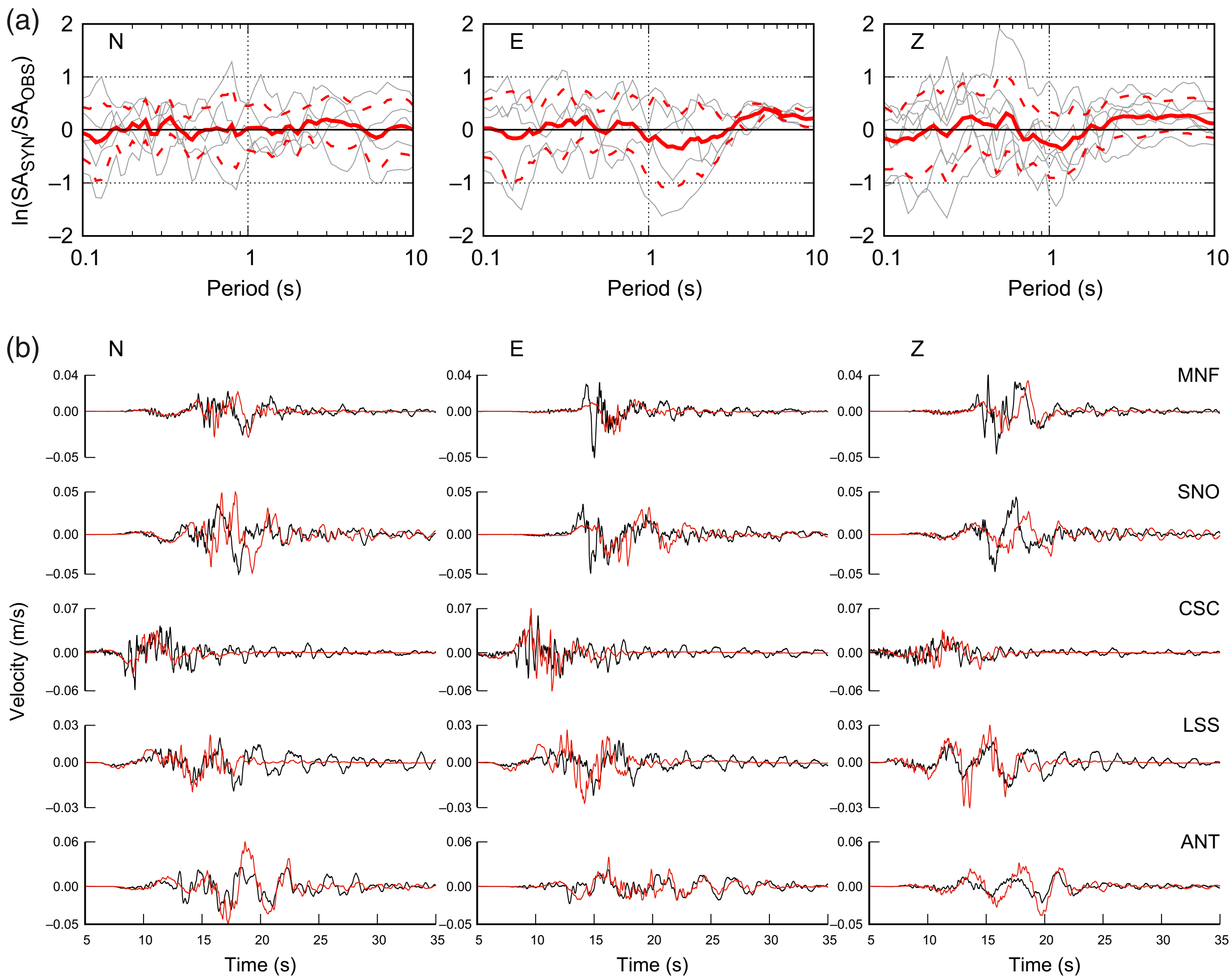

Figure 3. Comparison of ground motions of the optimal HIC model against real data at reference sites. (a) Spectral acceleration (SA) bias for each component as a function of the period between the observed and synthetic waveforms for the optimal model at the reference stations (gray lines). The red solid and dashed lines represent the mean and standard deviations over the stations, respectively. (b) Comparison of the observed (black line) and synthetic (red line) velocity waveforms for the optimal model at five reference stations. The color version of this figure is available only in the electronic edition.

demonstrates the increasing small-scale complexity in the path effects even at the reference stations (3D structures like sedimentary basins, topography, and scattering in fractured rocks). The high-frequency ground motions are generally more challenging to capture, although the stations are reference rock sites.

Figure 3b shows a relatively good fit between the observed and simulated velocity waveforms for the optimal model at five reference stations. We see a relatively good low-frequency waveform fit for stations LSS and CSC located perpendicularly to the rupture propagation. For station ANT oriented to the south, we observe long-period pulses resulting from the directivity both in the synthetics and observations. The waveforms at two stations toward the north, MNF and SNO, show similar pulses but with a temporal delay in the synthetics (see pulses in the later times at N and Z components). The latter can be assigned to different rupture velocities in the northern and southern parts of the rupture, as also indicated by the dynamic source inversion (Gallovič *et al.*, 2019), whereas modeled with a constant value in our present simplified simulations.

Ground-shaking prediction on rock sites

We simulate the ground motions for the optimal model at a regular grid of 400 virtual stations. Figure 4a shows the geometric mean of horizontal components of SAs at three frequencies, 0.5, 3, and 10 Hz (periods 2, 0.33, and 0.1 s), as a function of azimuth and Joyner–Boore distance (pinkish dots). Figure 4a also includes observations at reference stations (triangles), the remaining (nonreference) stations (circles), and synthetic values

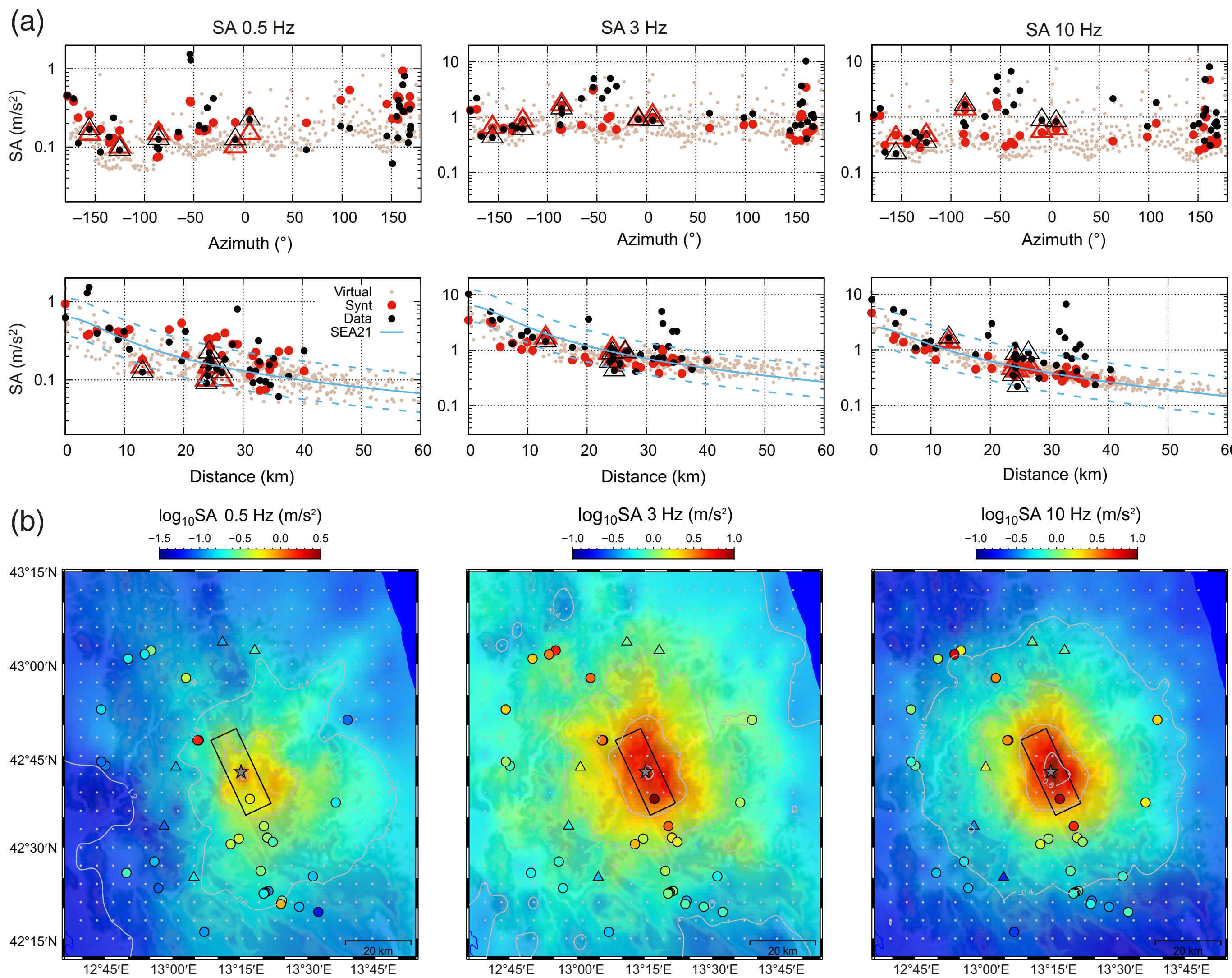

for the optimal model at all stations (red triangles and circles). The azimuthal dependence exhibits four lobes at ~90° intervals resulting from the source radiation pattern (note that this concerns mainly the more distant stations). This is consistent with the empirical observations of Kotha *et al.* (2019), who evidenced for normal faulting that ground-motion residuals show a four-lobed azimuthal trend, with minima in the strike-parallel (azimuths 155° and −25°) and strike-perpendicular directions (azimuths 65° and −115°), and maxima in between. We note that this pattern would be even stronger if we neglected the random variations of the subsource focal mechanisms in the composite part.

In the distance plots of Figure 4a, the synthetics and observations are supplemented by the prediction of the regional nonergodic GMM SEA21. The agreement between reference station observations, synthetics, and GMM is very good at all periods, including the variability. Moreover, the agreement is also good for most nonreference stations at the lowest frequencies (0.5 Hz) because the site effects are negligible. With decreasing periods, the variability of the simulations

Figure 4. Shaking distribution expressed by the geometric mean of horizontal components of simulated SAs at 0.5, 3, and 10 Hz for rock crustal models. (a) Geometric mean of horizontal SAs as a function of the azimuth (top) and distance (bottom) from the source. The black triangles and dots represent the peak values observed at reference and nonreference stations, respectively. The red triangles and dots show the corresponding synthetic values, and pinkish dots correspond to the simulations on a grid of 400 virtual stations around the fault (see Fig. 1a). The blue curves show the median and standard deviations of predictions by the GMM of Sgobba *et al.* (2021, SEA21). (b) The SA maps are interpolated from the predictions at virtual stations (pink points). The black rectangle shows the fault and the star depicts the epicenter. The triangles and circles show corresponding color-coded observed values at the real reference and nonreference stations, respectively. The simulated SAs agree with the observations at the reference sites. The simulated SAs are underestimated at higher frequencies (3 and 10 Hz) at nonreference stations due to the unaccounted site effects. The color version of this figure is available only in the electronic edition.

decreases when compared to GMM. This is because our 1D crustal models are too simple to account for complex 3D small-scale path and site effects on the variability (Pitarka, Akinci, *et al.*, 2021). The simulations agree with the median prediction of GMM at 10 Hz. At 3 Hz, the simulations underestimate SEA21 at distances shorter than 30 km while showing a good fit at larger distances. This may indicate inaccuracies in the GMM model in the near-source region because it is mainly constrained by observations at larger distances where the recordings are more abundant.

Figure 4b presents the map view of the simulated geometric mean of horizontal components of SAs at the same frequencies (i.e., the spatial distribution of shaking at bedrock) interpolated from the synthetics at the virtual stations. The maps illustrate the near-source features caused by the rupture process because site effects are not included. For example, the presence of a patch of relatively strong shaking near the epicenter reflects the slip asperity (Fig. 2c). The spatial pattern also agrees with the observed directivity at the Amatrice town to the south-southeast edge of the fault projection (Fig. 4b, left) where low-frequency pulses (about 0.5 Hz) at the AMT station have been recorded. This effect is indeed well captured by the low-frequency shaking that includes seismic wave coherency in the synthetics. At higher frequencies (3 and 10 Hz, Fig. 4b), an asymmetric distribution of the shaking can be noticed, with slightly larger values toward the north-northeast region (Adriatic coast), perhaps due to the footwall (i.e., radiation pattern) effect.

Figure 4b also includes the observed values at all (reference and nonreference) stations. The predicted and simulated values at reference stations agree relatively well for all the frequencies, whereas the simulations substantially underestimate the observed values at nonreference sites (also evidenced in Fig. 4a). Therefore, to provide more realistic estimates, the synthetic ground motions need to be supplemented by site contribution at nonreference stations.

Ground shaking at nonreference sites

To explore the performance of the broadband simulations and site-effect modeling at the nonreference stations, we apply the empirical site corrections $\delta S2S$ of SEA24, introduced above, to the synthetics calculated for rock conditions, where available. We apply both the mean site amplifications $\delta S2S$, as well as the $\delta S2S$ corrected for the event-specific effects δW_0, with reference to the Amatrice earthquake (Colavitti *et al.*, 2022; Sgobba *et al.*, 2024). The latter represents the leftover residuals between the recordings of the Amatrice earthquake and the nonergodic GMM containing the systematic source, path, and site effects. We include the event-specific residuals δW_0 (i.e., Amatrice specific contribution) because the local amplifications may not be completely separated from the source and path effects, which is often expressed as increased variability of the empirical site response terms. Indeed, the site-average response (i.e., the $\delta S2S$ calculated as the arithmetic mean from many events) can differ from the event-specific amplifications due to the source-site configuration, station topographical conditions or other site and propagation effects (Lanzano *et al.*, 2017; Pilz *et al.*, 2022).

The resulting SAs are compared in Figure 5a for a subset of 12 stations characterized by different source-to-site azimuths, including two near-source stations (AMT and NRC) and one reference rock site (MNF) for comparison (see Fig. S4 for the remaining stations). We also show the prediction by SEA21 including all source-, site-, and path-specific terms. Overall, the comparison between observed, corrected synthetic SAs, and SEA21 prediction is good.

At AMT, the corrected SAs agree well with observations, whereas SEA21 underestimates them at higher frequencies. On the contrary, at NRC located in a large basin (Luzi *et al.*, 2019), the corrections amplify the synthetic spectrum over the whole frequency range, but do not fully explain the observed data at frequencies below 2 Hz and the prominent peak at 5 Hz, perhaps due to a missing localized slip patch and/or complex interactions between source and basin. At the reference site MNF, the simulated, corrected, SEA21, and observations agree well, confirming the consistency of the empirical and numerical models. The SAs for stations SPM and TRE, located west of the fault, are strongly affected by site amplifications and agree with observations only when the mean and Amatrice-specific site corrections are included, except for the 6 Hz peak at the station SPM which, although present in the data, is overestimated in the the synthetics by both types of corrections. For most stations (FOS, ASP, TER, and AQV), the site correction is significant at frequencies above 2 Hz. The discrepancies at lower frequencies (see stations FOS and ASP) may indicate an improper crustal model used for the wave propagation simulation.

For most cases shown in Figure 5a, the synthetic predictions corrected for the average site effect ($\delta S2S$) are very close to that obtained by applying the Amatrice-specific correction ($\delta S2S + \delta W_0$). On the other hand, in some cases, the specific corrections show (frequency-dependent) discrepancies from the average. For instance, at station GSA located on a relief, where the topography affects the site response depending on the source-to-site path, we see that the synthetics with Amatrice-specific site corrections are much closer to the observation. Similarly, the CTD station shows local effects better captured by the $\delta S2S + \delta W_0$ correction, most likely due to peculiar installation effects and soil–structure interaction (the station is located inside an electrical cabin). At AQV situated in the valley, the site-corrected spectrum is very close except for the peak at ~3 Hz generated by the rock-site simulations, but then overamplified by the mean site correction. At the CLF station located in a basin, the SAs with mean site correction $\delta S2S$ underestimate the observations in the whole frequency range. Contrarily, the $\delta S2S + \delta W_0$ site correction reproduces the observed basin resonances better for

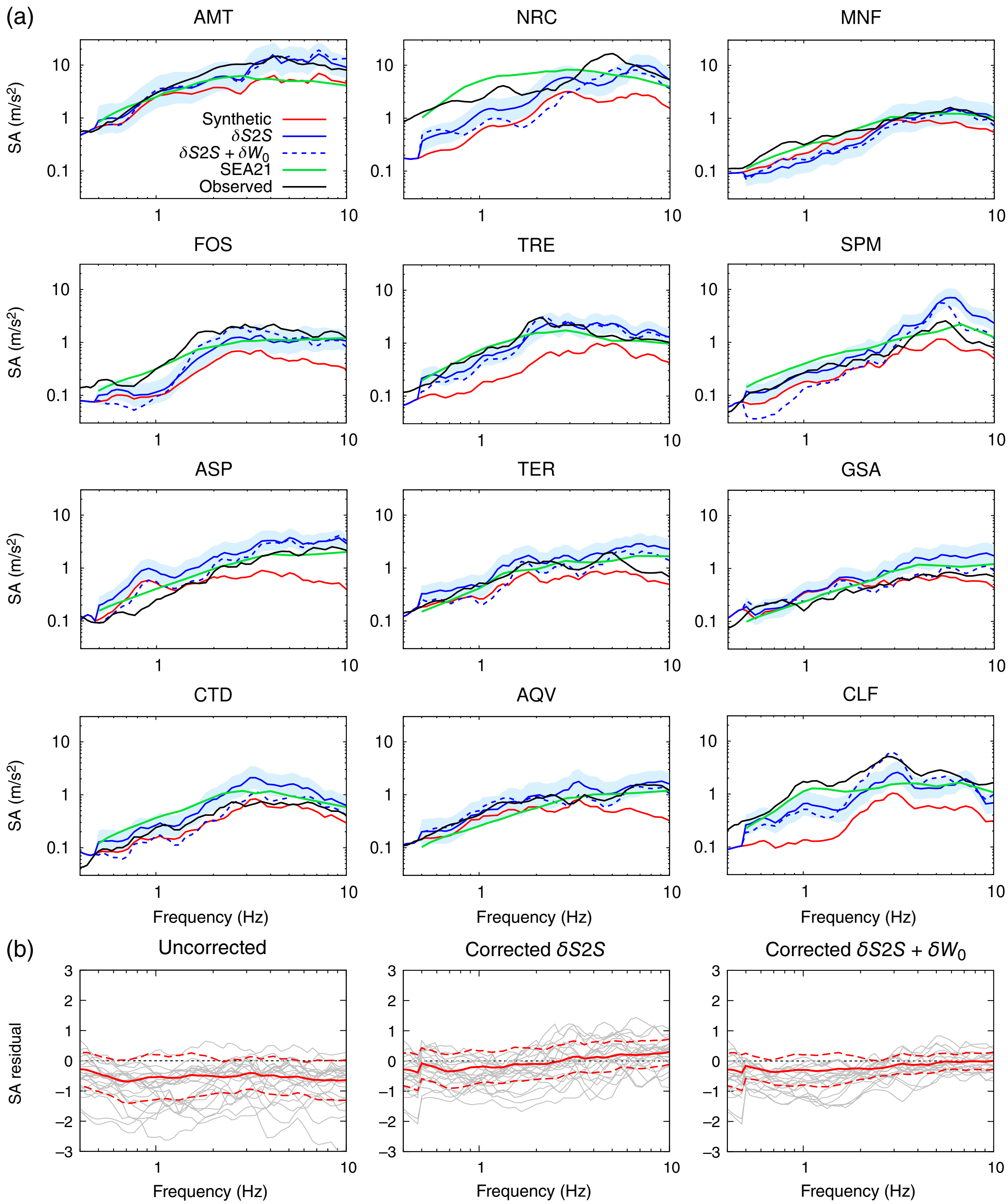

Figure 5. (a) Examples of site-corrected SAs at (non)reference stations (see also Fig. S5 for the full set). The black curves show the observed SAs, red lines correspond to the SAs simulated using the 1D rock site crustal models. The blue solid lines are synthetic SAs after applying mean site-correction $\delta S2S$ and blue-shaded region marks their uncertainty in terms of ±1 standard deviation. The blue dashed curves show site-corrected SAs assuming both mean site-term $\delta S2S$ and Amatrice-specific residual δW_0. The green curves show the GMM prediction by Sgobba *et al.* (2021) including source, path, and site terms. (b) SA bias of geometric mean of horizontal components for all the stations (including the nonreference stations) between observations and (left) simulations on rock site without empirical site corrections; (center) simulations corrected using the mean site-specific terms ($\delta S2S$); (right) simulations corrected using the site-specific ($\delta S2S$) and residual (δW_0) terms. The gray curves show the SA residuals for each station, red solid and dashed lines show the mean and standard deviations, respectively. The color version of this figure is available only in the electronic edition.

frequencies >1 Hz, whereas the peak at 1 Hz is underestimated. In this case, the complex valley edge effects may occur, whereby valley resonances are amplified or not depending on the portion of the basin traversed by the seismic waves. This effect is probably caused by an impedance and velocity contrast between the soft sedimentary coverage of the basin and the underlying bedrock, as found by borehole investigations (Pischiutta *et al.*, 2016). These 2D/3D effects and resonances at low frequencies could also be responsible for surface-wave generation in the coda portion of the recordings. However, such an effect cannot be captured by the specific amplification response $\delta S2S + \delta W_0$, which is instead calculated by the empirical site curve only on the S phase of the signal (Sgobba *et al.*, 2021), thus not taking into account the later arriving surface waves.

For the sake of completeness, Figure 5b shows the bias calculated for the geometric mean of the horizontal SAs for all stations using the original simulations on rock, SAs corrected by site-specific term $\delta S2S$, and SAs corrected by the Amatrice-specific amplification using both $\delta S2S$ and δW_0 terms. The underestimation by the rock-site simulations over all the frequencies is improved by applying the $\delta S2S$ corrections. We see a weak overestimation of the observations only at the highest frequencies. The SA bias variability decreases when applying the $\delta S2S$ corrections, and moreover, when including the Amatrice-specific correction δW_0, we observe a very good fit to data and a very low variability for frequencies above 2 Hz. This confirms that the residual term δW_0 can be a good proxy for the source-specific site amplification at higher frequencies unaccounted for in the simulations.

Discussion and Conclusions

We have validated the kinematic HIC broadband source model of the M_w 6.2 Amatrice earthquake by fitting the observed spectral accelerations between 0 and 10 Hz at reference rock stations (i.e., with weak or no site effects). We found the optimal ranges for rupture velocity and parameter a controlling the high-frequency radiation. However, these parameters show a trade-off indicating that the observed ground motions are constrained primarily by the event corner frequency aggregating the two parameters. We inspected the synthetic ground motions generated by the optimal HIC model and compared them with predictions of the regional nonergodic model by Sgobba *et al.* (2021). For the reference rock sites, we see a good agreement with observations and empirical model in the far field, showing the potential of the simulations to replace and/or integrate the uneven or missing near-source observations.

The presented validation is an important step before the construction of ground-shaking scenarios because it may reveal the important ingredients for reproducing with greater accuracy the spatial anisotropy of the near-source ground motions related not only to the rupture mechanisms. For example, to generate realistic M_w 6.2 rupture scenarios on the Amatrice fault by the HIC method in Čejka *et al.* (2024), we have adopted the same fault orientation, the two regional crustal models and the crossover frequency range and varied the fault size, slip distribution, nucleation position, rupture velocity v_r, and parameter a, and explored the effects of the individual source parameters on the ground-motion variability.

To improve the modeling at nonreference stations (i.e., stations with significant site effects), we have applied the empirically derived site corrections to the synthetic SAs (simulated for reference rock conditions) for all available stations. We note that the additional source model validation at nonreference sites may unveil any missing features of the source model only after the site correction is applied to the synthetics. The general underestimation observed in the rock-site simulations over all the frequencies is improved when applying the empirically derived site corrections, suggesting their ability to capture local features due to topography, installation conditions, impedance contrasts, and effects related to source-site configuration. The remaining deficiencies are likely related to the very complex local structure (such as basin-edge-induced surface waves). They can thus hardly be explained without 3D wave propagation modeling and perfect knowledge of the velocity model. Despite this, when we optimize the kinematic source model on a good set of reference stations, we can provide fast, realistic estimates of ground motions by applying empirical site corrections to the synthetic ground-motion spectra calculated in simple crustal models.

The proposed method is an example of how synthetic and empirical site predictions can be combined. This is a key aspect because, in practical use, simulations must be adjusted to consider site effects, which are one of the primary contributors to ground-shaking variability, especially in areas with complex geomorphology. More generally, providing synthetic time series that capture the distinct features of ground motion in a particular region, including proper crustal attenuation and soil response, can be helpful in engineering applications. This is especially useful when selecting near-source records compatible with a given design spectrum because strong-motion records at short epicentral distances of medium-to-large earthquakes are often scarce. As a result, they can be used as an input for dynamic structural analysis in engineering and geotechnical applications, providing valuable insights and contributing to the development of the seismic risk assessment and design scenario tools.

Data and Resources

All data and metadata related to the Amatrice event and stations used for the analyses were taken from the ITalian ACcelerometric Archive (ITACA) (https://itaca.mi.ingv.it/ItacaNet_32/#/home; Russo *et al.*, 2022) and the Engineering Strong-Motion (ESM) (https://esm-db.eu/#/home) database (Lanzano *et al.*, 2021). Both websites were last accessed in June 2024. The supplemental material includes Table S1 of referential stations with their detailed site information; Table S2 includes both velocity models; and Figure S1 show depth-dependent Q value; and Texts S1 and S2 summarize the effects of κ and crossover frequency range, respectively.

Declaration of Competing Interests

The authors acknowledge that there are no conflicts of interest recorded.

Acknowledgments

The authors appreciate the comments provided by A. Pitarka and an anonymous reviewer, which helped improve the article. The authors thank C. Mascandola for providing the velocity models of the Amatrice and Norcia areas. The authors acknowledge financial support from the Czech Science Foundation (Project Number 23-06345S), Charles University Project Number SVV 115–09/260581, and the Istituto Nazionale di Geofisica e Vulcanologia (INGV) "Ricerca Libera" 2021 Project Number HSE-GMM (S. Sgobba) "A Hybrid Simulation-Empirical approach to model variability of ground motion in near-source region". This research is also partially supported by INGV in the frame of the project SECURE (Regional-scale earthquake ground-motion predictions through pyhsics-based and empirical approaches: A case study Central Italy) within Pianeta Dinamico (Working Earth)—Geosciences for the Understanding of the Dynamics of the Earth and the Consequent Natural Risks (CUP code D53J19000170001) funded by the Italian Ministry of University and Research (MIUR).

References

Akinci, A., H. Aochi, A. Herrero, M. Pischiutta, and D. Karanikas (2017). Physics-based broadband ground-motion simulations for probable Mw≥7.0 earthquakes in the Marmara Sea region (Turkey), *Bull. Seismol. Soc. Am.* **107,** no. 3, 1307–1323, doi: 10.1785/0120160096.

Ameri, G., A. Emolo, F. Pacor, and F. Gallovič (2011). Ground-motion simulations for the 1980 M 6.9 Irpinia earthquake (southern Italy) and scenario events, *Bull. Seismol. Soc. Am.* **101,** no. 3, 1136–1151.

Ameri, G., F. Gallovič, and F. Pacor (2012). Complexity of the M_w 6.3 2009 L'Aquila (central Italy) earthquake: 2. Broadband strong-motion modeling, *J. Geophys. Res.* **117,** no. B4, doi: 10.1029/2011JB008729.

Ameri, G., F. Gallovič, F. Pacor, and A. Emolo (2009). Uncertainties in strong ground-motion prediction with finite-fault synthetic seismograms: An application to the 1984 M 5.7 Gubbio, central Italy, earthquake, *Bull. Seismol. Soc. Am.* **99,** no. 2A, 647–663, doi: 10.1785/0120080240.

Anderson, J. G., and S. Hough (1984). A model for the shape of the Fourier amplitude spectrum of acceleration at high frequencies, *Bull. Seismol. Soc. Am.* **74,** 1969–1984.

Bard, P. Y., S. S. Bora, F. Hollender, A. Laurendeau, and P. Traversa (2020). Are the standard Vs30-kappa host-to-target adjustments the only way to get consistent hard-rock ground motion prediction? *Pure Appl. Geophys.* **177,** 2049–2068.

Bianchi, I., C. Chiarabba, and N. P. Agostinetti (2010). Control of the 2009 L'Aquila earthquake, central Italy, by a high-velocity structure: A receiver function study, *J. Geophys. Res.* **115,** no. B12, doi: 10.1029/2009JB007087.

Bradley, B., D. Pettinga, J. Baker, and J. Fraser (2017). Guidance on the utilization of earthquake-induced ground motion simulations in engineering practice, *Earthq. Spectra* **33,** doi: 10.1193/120216eqs219ep.

Brune, J. N. (1970). Tectonic stress and the spectra of seismic shear waves from earthquakes, *J. Geophys. Res.* **75,** no. 26, 4997–5009, doi: 10.1029/JB075i026p04997.

Calderoni, G., and R. E. Abercrombie (2023). Investigating spectral estimates of stress drop for small to moderate earthquakes with heterogeneous slip distribution: Examples from the 2016–2017 Amatrice earthquake sequence, *J. Geophys. Res.* **128,** e2022JB025022, doi: 10.1029/2022JB025022.

Castro, R., L. Colavitti, C. Vidales-Basurto, F. Pacor, S. Sgobba, and G. Lanzano (2022). Near-source attenuation and spatial variability of the spectral decay parameter kappa in central Italy, *Seism. Res. Lett.* **93,** 2299–2310.

Čejka, F., S. Sgobba, F. Pacor, C. Felicetta, Ľ. Valentová, and F. Gallovič (2024). Constraining between-event variability of kinematic rupture scenarios by empirical ground-motion model: A case study in central Italy, *Bull. Seismol. Soc. Am.* doi: 10.1785/0120230251.

Čejka, F., J. Zahradník, F. Turhan, E. Sokos, and F. Gallovič (2023). Long-period directivity pulses of strong ground motion during the 2023 M_w 7.8 Kahramanmaraş earthquake, *Commun. Earth Environ.* **4,** 413, doi: 10.1038/s43247-023-01076-x.

Chiaraluce, L., R. Di Stefano, E. Tinti, L. Scognamiglio, M. Michele, E. Casarotti, M. Cattaneo, P. De Gori, C. Chiarabba, G. Monachesi, *et al.* (2017). The 2016 central Italy seismic sequence: A first look at the mainshocks, aftershocks, and source models, *Seismol. Res. Lett.* **88,** no. 3, 757–771, doi: 10.1785/0220160221.

Cirella, A., G. Pezzo, and A. Piatanesi (2018). Rupture kinematics and structural-rheological control of the 2016 M_w 6.1 Amatrice (central Italy) earthquake from joint inversion of seismic and geodetic data, *Geophys. Res. Lett.* **45,** 12,302–12,311, doi: 10.1029/2018GL080894.

Colavitti, L., G. Lanzano, S. Sgobba, F. Pacor, and F. Gallovič (2022). Empirical evidence of frequency-dependent directivity effects from small-to-moderate normal fault earthquakes in central Italy, *J. Geophys. Res.* **127,** e2021JB023498, doi: 10.1029/2021JB023498.

Cotton, F., and O. Coutant (1997). Dynamic stress variations due to shear faults in a plane-layered medium, *Geophys. J. Int.* **128,** no. 3, 676–688, doi: 10.1111/j.1365-246X.1997.tb05328.x.

Felicetta, C., C. Mascandola, D. Spallarossa, F. Pacor, S. Hailemikael, and G. Di Giulio (2021). Quantification of site effects in the Amatrice area (central Italy): Insights from ground-motion recordings of the 2016–2017 seismic sequence, *Soil Dynam. Earthq. Eng.* **142,** 106565, doi: 10.1016/j.soildyn.2020.106565.

Galli, P., E. Peronace, and A. Tertulliani (2016). *Rapporto sugli effetti macrosismici del terremoto del 24 agosto 2016 di Amatrice in scala MCS*, Rapporto congiunto DPC, CNRIGAG, Rome, Italy, 15 pp., doi: 10.5281/zenodo.161323 (in Italian).

Gallovič, F. (2016). Modeling velocity recordings of the M_w 6.0 South Napa, California, earthquake: unilateral event with weak high-frequency directivity, *Seismol. Res. Lett.* **87,** 2–14.

Gallovič, F., and J. Brokešová (2007). Hybrid k-squared source model for strong ground motion simulations: Introduction, *Phys. Earth Planet. In.* **160,** 34–50, doi: 10.1016/j.pepi.2006.09.002.

Gallovič, F., and Ľ. Valentová (2023). Broadband strong ground motion modeling using planar dynamic rupture with fractal parameters, *J. Geophys. Res.* **128,** e2023JB026506, doi: 10.1029/2023JB026506.

Gallovič, F., G. Ameri, J. Zahradník, J. Janský, V. Plicka, E. Sokos, A. Askan, and M. Pakzad (2013). Fault process and broadband ground-motion simulations of the October 23 2011 Van (eastern Turkey) earthquake, *Bull. Seismol. Soc. Am.* **103,** 3164–3178.

Gallovič, F., Ľ. Valentová, J.-P. Ampuero, and A.-A. Gabriel (2019). Bayesian dynamic finite-fault inversion: 2. Application to the 2016 M_w 6.2 Amatrice, Italy, earthquake, *J. Geophys. Res.* **124,** 6970–6988.

Graves, R., and A. Pitarka (2010). Broadband ground-motion simulation using a hybrid approach, *Bull. Seismol. Soc. Am.* **100,** 2095–2123.

Graves, R., T. H. Jordan, S. Callaghan, E. Deelman, E. Field, G. Juve, C. Kesselman, P. Maechling, G. Mehta, K. Milner, *et al.* (2011). CyberShake: A physics-based seismic hazard model for southern California, *Pure Appl. Geophys.* **168,** 367–381.

Kemna, K. B., A. Verdecchia, and R. M. Harrington (2021). Spatio-temporal evolution of earthquake static stress drop values in the 2016–2017 central Italy seismic sequence, *J. Geophys. Res.* **126,** no. 11, e2021JB022566, doi: 10.1029/2021JB022566.

Kotha, S. R., F. Cotton, and D. Bindi (2019). Empirical models of shear-wave radiation pattern derived from large datasets of ground-shaking observations, *Sci. Rep.* **9,** 981, doi: 10.1038/s41598-018-37524-4.

Lanzano, G., M. D'Amico, C. Felicetta, L. Luzi, and R. Puglia (2017). Update of the single-station sigma analysis for the Italian strong-motion stations, *Bull. Earthq. Eng.* **15,** 2411–2428, doi: 10.1007/s10518-016-9972-x.

Lanzano, G., C. Felicetta, F. Pacor, D. Spallarossa, and P. Traversa (2020). Methodology to identify the reference rock sites in regions of medium-to-high seismicity: An application in central Italy, *Geophys. J. Int.* **222,** 2053–2067, doi: 10.1093/gji/ggaa261.

Lanzano, G., C. Felicetta, F. Pacor, D. Spallarossa, and P. Traversa (2022). Generic-to-reference rock scaling factors for seismic ground motion in Italy, *Bull. Seismol. Soc. Am.* **112,** no. 3, 1583–1606, doi: 10.1785/0120210063.

Lanzano, G., L. Luzi, C. Cauzzi, J. Bienkowski, D. Bindi, J. Clinton, M. Cocco, M. D'Amico, J. Douglas, L. Faenza, *et al.* (2021). Accessing European strong-motion data: An update on ORFEUS coordinated services, *Seismol. Res. Lett.* **92,** 1642–1658, doi: 10.1785/0220200398.

Loviknes, K., S. R. Kotha, F. Cotton, and D. Schorlemmer (2021). Testing nonlinear amplification factors of ground-motion models, *Bull. Seismol. Soc. Am.* **111,** no. 4, 2121–2137, doi: 10.1785/0120200386.

Luzi, L., M. D'Amico, M. Massa, and R. Puglia (2019). Site effects observed in the Norcia intermountain basin (central Italy) exploiting a 20-year monitoring, *Bull. Earthq. Eng.* **17,** 97–118, doi: 10.1007/s10518-018-0444-3.

Mai, P., and G. C. Beroza (2003). A hybrid method for calculating near-source, broadband seismograms: Application to strong motion prediction, *Phys. Earth Planet. In.* **137,** 183–199.

McCallen, D., F. Petrone, M. Miah, A. Pitarka, A. Rodgers, and N. Abrahamson (2021). EQSIM—A multidisciplinary framework for fault-to-structure simulations on exascale computers Part II: Regional simulations of building response, *Earthq. Spectra* **37,** no. 2, 736–761.

Morasca, P., D. Bindi, K. Mayeda, J. Roman-Nieves, J. Barno, W. R. Walter, and D. Spallarossa (2022). Source scaling comparison and validation in central Italy: Data intensive direct S waves versus the sparse data coda envelope methodology, *Geophys. J. Int.* **231,** no. 3, 1573–1590.

Morasca, P., W. R. Walter, K. Mayeda, and M. Massa (2019). Evaluation of earthquake stress parameters and its scaling during the 2016-2017 Amatrice-Norcia-Visso sequence—Part I, *Geophys. J. Int.* **218,** no. 1, 446–455, doi: 10.1093/gji/ggz165.

Ojeda, J., A. Akinci, E. Tinti, S. Arriola, and S. Ruiz (2021). Hybrid broadband strong-motion simulation to investigate the near-source characteristics of the M 6.5, 30 October 2016 Norcia, Italy earthquake, *Soil Dynam. Earthq. Eng.* **149,** 106866, doi: 10.1016/j.soildyn.2021.106866.

Pacor, F., F. Gallovič, R. Puglia, L. Luzi, and M. D'Amico (2016). Diminishing high-frequency directivity due to a source effect: Empirical evidence from small earthquakes in the Abruzzo region, Italy, *Geophys. Res. Lett.* **43,** no. 10, 5000–5008

Paolucci, R., F. Gatti, M. Infantino, C. Smerzini, A. G. Özcebe, and M. Stupazzini (2018). Broadband ground motions from 3D physics-based numerical simulations using artificial neural networks, *Bull. Seismol. Soc. Am.* **108,** no. 3A, 1272–1286, doi: 10.1785/0120170293.

Paolucci, R., C. Smerzini, and M. Vanini (2021). BB-SPEEDset: A validated dataset of broadband near-source earthquake ground motions from 3D physics-based numerical simulations, *Bull. Seismol. Soc. Am.* **111,** no. 5, 2527–2545.

Pilz, M., F. Cotton, and C. Zhu (2022). How much are sites affected by 2-D and 3-D site effects? A study based on single-station earthquake records and implications for ground motion modelling, *Geophys. J. Int.* **228,** no. 3, 1992–2004, doi: 10.1093/gji/ggab454.

Pischiutta, M., A. Akinci, L. Malagnini, and A. Herrero (2016). Characteristics of the strong ground motion from the 24th August 2016 Amatrice earthquake, *Ann. Geophys.* **59,** doi: 10.4401/ag-7219.

Pischiutta, M., A. Akinci, E. Tinti, and A. Herrero (2021). Broad-band ground-motion simulation of 2016 Amatrice earthquake, central Italy, *Geophys. J. Int.* **224,** no. 3, 1753–1779, doi: 10.1093/gji/ggaa412.

Pitarka, A., A. Akinci, P. DeGori, and M. Buttinelli (2021). Deterministic 3D ground-motion simulations (0-5Hz) and surface topography effects of the 30 October 2016 M_w 6.5 Norcia, Italy earthquake, *Bull. Seismol. Soc. Am.* doi: 10.1785/0120210133.

Pitarka, A., R. Graves, K. Irikura, K. Miyakoshi, C. Wu, H. Kawase, A. Rodgers, and D. McCallen (2021). Refinements to the Graves–Pitarka kinematic rupture generator, including a dynamically consistent slip-rate function, applied to the 2019 M_w 7.1 Ridgecrest earthquake, *Bull. Seismol. Soc. Am.* **112,** no. 1, 287–306, doi: 10.1785/0120210138.

Pizzi, A., A. Di Domenica, F. Gallovič, L. Luzi, and R. Puglia (2017). Fault segmentation as constraint to the occurrence of the main shocks of the 2016 central Italy seismic sequence, *Tectonics* **36,** 2370–2387, doi: 10.1002/2017TC004652.

Razafindrakoto, H. N. T., B. A. Bradley, and R. W. Graves (2018). Broadband ground-motion simulation of the 2011 M_w 6.2 Christchurch, New Zealand, earthquake, *Bull. Seismol. Soc. Am.* **108,** no. 4, 2130–2147, doi: 10.1785/0120170388.

Russo, E., C. Felicetta, M. D'Amico, S. Sgobba, G. Lanzano, C. Mascandola, F. Pacor, and L. Luzi (2022). Italian Accelerometric Archive v3.2—Istituto Nazionale di Geofisica e Vulcanologia, Dipartimento della Protezione Civile Nazionale, doi: 10.13127/itaca.3.2 (in Italian).

Sgobba, S., C. Felicetta, T. Bortolotti, A. Menafoglio, G. Lanzano, and F. Pacor (2024). A geostatistical modelling of empirical amplification functions and related site proxies for shaking scenarios in central Italy, *Soil Dynam. Earthq. Eng.* **179,** 108496, doi: 10.1016/j.soildyn.2024.108496.

Sgobba, S., G. Lanzano, and F. Pacor (2021). Empirical nonergodic shaking scenarios based on spatial correlation models: An application to central Italy, *Earthq. Eng. Struct. Dynam.* **50,** no. 1, 60–80, doi: 10.1002/eqe.3362.

Supino, M., G. Festa, and A. Zollo (2019). A probabilistic method for the estimation of earthquake source parameters from spectral inversion: application to the 2016–2017 central Italy seismic sequence, *Geophys. J. Int.* **218,** no. 2, 988–1007.

Taufiqurrahman, T., A.-A. Gabriel, T. Ulrich, Ľ. Valentová, and F. Gallovič (2023). Broadband dynamic rupture modeling with fractal fault roughness, frictional heterogeneity, viscoelasticity and topography: The 2016 M_w 6.2 Amatrice, Italy earthquake, *Geophys. Res. Lett.* **49,** e2022GL098872, doi: 10.1029/2022GL098872.

Tinti, E., L. Scognamiglio, A. Michelini, and M. Cocco (2016). Slip heterogeneity and directivity of the M_L 6.0, 2016, Amatrice earthquake estimated with rapid finite-fault inversion, *Geophys. Res. Lett.* **43,** 10,745–10,752, doi: 10.1002/2016GL071263.

Valentová, Ľ., F. Gallovič, and S. Hok (2021). Near-source ground motions and their variability derived from dynamic rupture simulations constrained by NGA-West2 GMPEs, *Bull. Seismol. Soc. Am.* **111,** no. 5, 2559–2573, doi: 10.1785/0120210073.

Manuscript received 5 December 2023
Published online 19 July 2024